processes

MDPI

Article

Improvement of Catalytic Activity of Platinum Nanoparticles Decorated Carbon Graphene Composite on Oxygen Electroreduction for Fuel Cells

Halima Begum and Young-Bae Kim *

Department of Mechanical Engineering, Chonnam National University, Gwangju 61186, Korea
* Correspondence: ybkim@chonnam.ac.kr

Received: 14 August 2019; Accepted: 23 August 2019; Published: 3 September 2019

Abstract: High-performance platinum (Pt)-based catalyst development is crucially important for reducing high overpotential of sluggish oxygen reduction reaction (ORR) at Pt-based electrocatalysts, although the high cost and scarcity in nature of Pt are profoundly hampering the practical use of it in fuel cells. Thus, the enhancing activity of Pt-based electrocatalysts with minimal Pt-loading through alloy, core−shell or composite making has been implemented. This article deals with enhancing electrocatalytic activity on ORR of commercially available platinum/carbon (Pt/C) with graphene sheets through a simple composite making. The Pt/C with graphene sheets composite materials (denoted as Pt/C_x:G_{10-x}) have been characterized by several instrumental measurements. It shows that the Pt nanoparticles (NPs) from the Pt/C have been transferred towards the π-conjugated systems of the graphene sheets with better monolayer dispersion. The optimized Pt/C_8:G_2 composite has higher specific surface area and better degree of graphitization with better dispersion of NPs. As a result, it shows not only stable electrochemical surface area but also enhanced ORR catalytic activity in respect to the onset potential, mass activity and electron transfer kinetics. As shown by the ORR, the Pt/C_8:G_2 composite is also better resistive to the alcohol crossover effect and more durable than the Pt/C.

Keywords: composite; fuel cells; graphene; oxygen reduction reaction; platinum carbon

1. Introduction

The sluggish kinetics of four electron involved electrocatalytic oxygen reduction reaction (ORR) in an acidic environment is a major obstacle for the development of cost effective fuel cells (FCs) [1–4]. The development of catalysts with high activity for the ORR is essential to proton exchange membrane fuel cells (PEMFCs), since the majority of activation losses occur at the cathode and it turns into an interesting research area [1–7]. The platinum (Pt)-based materials have been regarded as the most efficient electrocatalyst for ORR [8–11] because of the excellent ORR catalytic activity. Carbon supported Pt (Pt/C) is typically utilized as the state-of-the-art ORR catalyst, but is inadequate for the combined cost, performance and durability requirements [12–15]. To promote the development of highly active ORR catalysts, the United States Department of Energy sets the target as mass activity (MA, the catalytic activity per given mass of Pt, 0.44 A mg^{-1}, 2017–2020) [16,17]. Currently, the high cost of Pt becomes the primary limiting factor preventing the widespread adoption of FCs [18–20], thus, the high Pt-MA must be achieved. However, the MA is determined by the specific activity (SA, normalized by surface area) and the electrochemically active surface area (ECSA, normalized by mass), which can be optimized by tuning the exposed catalytic site on catalyst surface [21–23]. Therefore, several challenges, such as the lowering amount of Pt-loading in the cathode, preventing Pt nanoparticles (NPs) from severe dissolution and/or migration and corrosion of carbon substrate during

electrochemical processes must be overcome for improving catalytic activity of Pt-based catalysts, i.e., Pt/C. There are several methods have been implemented including alloy, core−shell or composite making for reducing Pt-loading and dissolution in the cathode [24–26].

Graphene (G), as a two-dimensional (2D) sp^2-carbon network sheet, has received a great attention in scientific community in the applications of energy storage and conversion, owing to the properties of theoretically large specific surface area, excellent electrical conductivity and high mechanical strength [27–31]. Experimentally, however, the surface areas of G-based materials are far below this value because of the strong self-aggregation/stacking tendency. To prevent the aggregation of graphene, many researchers are trying to design a three-dimensional (3D) structure [32,33] or make composites with carbon materials [34–37] that could facile the ORR performance as well [34,37]. This is due to the synergistic contributions of large surface area and π-electron-rich sp^2-G sheets [37] and the non-precious particulate-like sp^3-carbon [38]. Additionally, it has been reported that the sp^3-C-rich G-sheets could provide efficient catalysis to ORR because of their effective charge polarization ability [39–41], which strongly indicates that the composition of sp^3-carbon and sp^2-G could have significant effect on the development of cost effective and efficient ORR catalysts for FCs [34,42].

Based on the above discussions, a simple strategy has been applied to improve catalytic activity and durability of commercially available Pt/C with the limited addition of G-sheets ($Pt/C_x:G_{10-x}$). The $Pt/C_x:G_{10-x}$ composite has been employed successfully for electrochemical ORR catalysis. The optimized composite, $Pt/C_8:G_2$, showed a higher and more stable electrochemical surface area (ECSA) and enhanced ORR catalytic activity in respect to the onset potential, MA and electron transfer kinetics in acid media than that of Pt/C, which result from higher specific surface area (SSA) and better degree of graphitization with better dispersion of Pt NPs. Therefore, the as-prepared $Pt/C_8:G_2$ composite is demonstrated to be a promising cost effective, highly efficient and stable ORR electrocatalyst.

2. Materials and Methods

2.1. Material Synthesis

For the preparation of $Pt/C_x:G_{10-x}$, 50 mg of 20 wt% Pt/C (E-TEK) was taken in a 100 mL vial, followed by the addition of 70 mL water under vigorous stirring. Under continuous stirring, 1 mg mL^{-1} of Graphene oxide (GO) solution (mass ratio of Pt/C:G was, x:10−x, where x = 10 to 1) was added slowly and stirred for next 30 min. Afterwards, 10 mL of 0.1 M $NaBH_4$ was added to the above solution and refluxed at 100 °C for 12 h. The solution was then filtered and washed with water three times. The as-obtained $Pt/C_x:G_{10-x}$ was then dried at 60 °C for 12 h in a vacuum oven. For comparison, G-sheets catalyst was prepared with the same process without addition of Pt/C.

2.2. Electrochemical Characterization

A 10 µL of G, $Pt/C_x:G_{10-x}$ or Pt/C suspension in ethanol (1 mg mL^{-1} with 5 µL of 5% Nafion solution) was dropped onto the prepolished glassy carbon electrode (GCE, geometric area: 0.0707 cm^2). All electrochemical techniques including cyclic voltammetry (CV), linear sweep voltammetry (LSV) and chronoamperometry (CA) were performed using a three-electrode potentiostat [CHI 700C electrochemical workstation (U.S.A.)]. A Pt wire was used as auxiliary electrode and Ag/AgCl electrode was used as reference electrode. The rotating ring disk electrode (RRDE) measurements were done using an EG&G Model 636 RDE system along with the CHI 700C. All electrochemical experiments were performed in high purity argon $(Ar)^-$ or $O_2{}^-$ purged (for at least 30 min) 0.1 M $HClO_4$ electrolyte. All potentials were calculated with respect to reversible hydrogen electrode (RHE) scale according to the Nernst equation ($E_{RHE} = E_{Ag/AgCl} + 0.059\ pH + E^{\circ}{}_{0.197\ V}$, at 25 °C).

3. Results and Discussions

3.1. Surface Analysis of Pt/C_x:G_{10-x}

The Pt/C_x:G_{10-x} including Pt/C and G-sheets were first characterized by transmission electron microscopy (TEM) analysis and the images of as-prepared composites are displaying in Figure 1. The TEM image of the G-sheets showed the typical thin film and nanosheets-like structure (Figure 1a). The G-sheets with a laminar characteristic assembled by a wrinkled silk veil were obtained after removal of oxygen functional groups form the surface due to reduction. The partially crinkled nature of G-sheets probably originated from the defective nature, which was generated from the reduction process of GO [27]. Pt/C (Figure 1b) and Pt/C_8:G_2 (Figure 1c) consist of clear crystal Pt NPs with spherical size and without any serious aggregation or agglomeration. The images of both samples are showing that the Pt NPs were mostly in uniform size within the range of 2 to 4 nm. The most striking feature is that the Pt NPs were migrated onto the surfaces of G-sheets (Figure 1d). For a better understanding, the high resolution TEM (HRTEM) images were also recorded, which show the migration of Pt NPs from Pt/C to G-sheets with excellent mono-dispersion that can greatly boost the electrocatalytic activity.

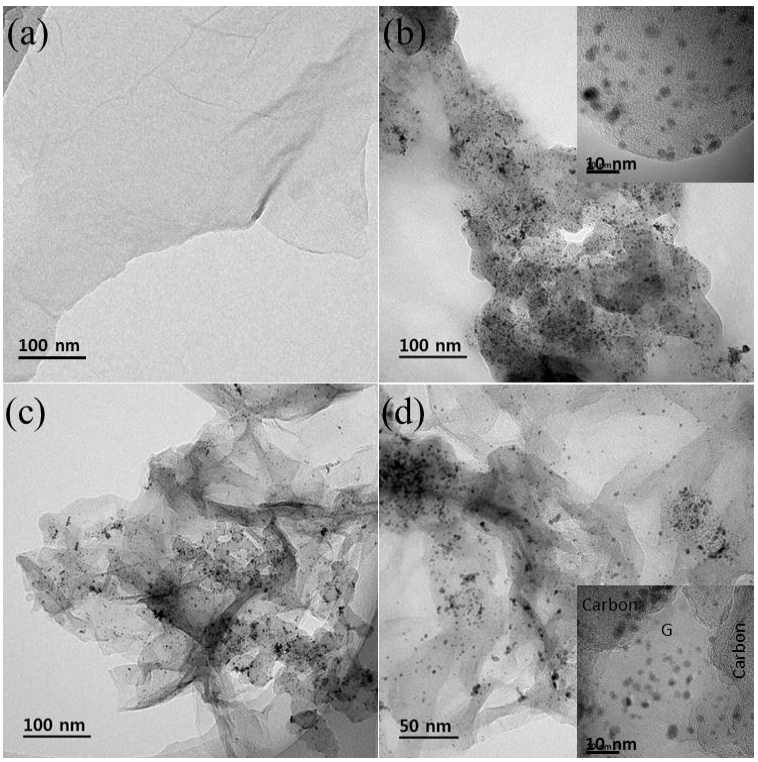

Figure 1. TEM images of G-sheets (**a**), Pt/C (**b**) and Pt/C_8:G_2 (**c**,**d**); insets: high resolution TEM (HRTEM) of Pt/C (**b**) and Pt/C_8:G_2 (**d**).

To understand the influence and optimization of G-sheets addition with Pt/C, the morphology has also been investigated as in Figure 2. Figure 2, shows the TEM images of Pt/C (a), Pt/C_8:G_2 (b), Pt/C_6:G_4 (c) and Pt/C_1:G_9 (d). All samples contained Pt NPs on carbon and G-sheets and the Pt NPs were transferred onto G-sheets upon simple addition. The TEM image of Pt/C showed that the higher density of NPs with such aggregation on carbon matrix (Figure 2a). Upon addition of 20% (*w*/*w*) of G-sheets, the Pt NPs were migrated onto G-sheets with aggregation-free distribution (Figure 2b). At 40% (*w*/*w*) addition, the Pt NPs were also migrated with lower amount in Figure 2c. For comparison, it is also observed that the Pt NPs were migrated with lower amount at the surface of

Pt/C_1:G_9 (Figure 2d). Therefore, as observed in Figures 1 and 2, the addition of 20% of G-sheets was optimal for the preparation of good quality of Pt/C_x:G_{10-x} with better Pt NPs dispersion morphology.

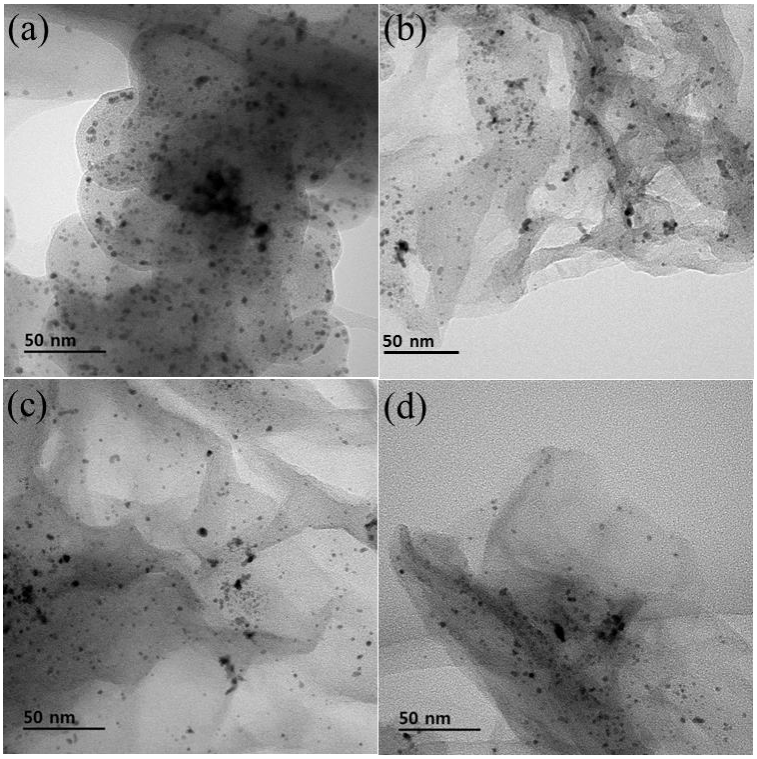

Figure 2. TEM images of Pt/C (**a**), Pt/C_8:G_2 (**b**), Pt/C_6:G_4 (**c**) and Pt/C_1:G_9 (**d**).

3.2. Raman Analysis of Pt/C_x:G_{10-x}

To investigate the internal structure of Pt/C_x:G_{10-x} composite, Raman spectroscopy was used, which is known as an important tool to investigate the graphitic, crystalline and electronic properties of carbon-based materials [43–45]. Characterization of carbon-based materials can be done by comparing D and G bands while the D band represents the disordered graphitic structure with a significant level of defects and the G band is related to the E_{2g} phonon of the ordered sp^2-graphitic structure. Therefore, the intensity ratio of D band and G band (I_D/I_G) is considered to reflect the relative disorder stemming from structural imperfection of graphitic structure. In Figure 3a, the narrow D band at 1351 cm^{-1} and strong G band at 1599 cm^{-1} were observed at G-sheets spectrum and the I_D/I_G was calculated as 0.88 which indicating the distortion in G-sheets [46]. Additionally, I_D/I_G was 0.99 for pristine Pt/C, indicating sp^3-C rich carbon black in Pt/C sample. The value was similar to the previous report [47]. After analyzing Raman data, the I_D/I_G was found to be increased from 0.88 (or 0.99) to 1.03 and 1.11 for Pt/C_6:G_4 and Pt/C_8:G_2, respectively, which indicated a better graphitization. Unlikely the G band of Pt/C (1597.5 cm^{-1}), G bands of Pt/C_8:G_2 (1598 cm^{-1}) and Pt/C_6:G_4 (1598.3 cm^{-1}) were up-shifted, which indicated a better composite formation in between C and G-sheets. Moreover, the intensity of 2D band from Raman spectroscopy indicates the multilayer stacking of G-sheets. However, the intensity of the 2D band was higher at Pt/C_6:G_4 than that at Pt/C_8:G_2 in Figure 3a that indicating better dispersion of Pt/C onto few layer G-sheets in Pt/C_8:G_2 sample compared to multilayer assembly of G-sheets in Pt/C_6:G_4 sample [48]. This feature could be facilitate to the SSA and subsequent electrocatalytic activity [48,49].

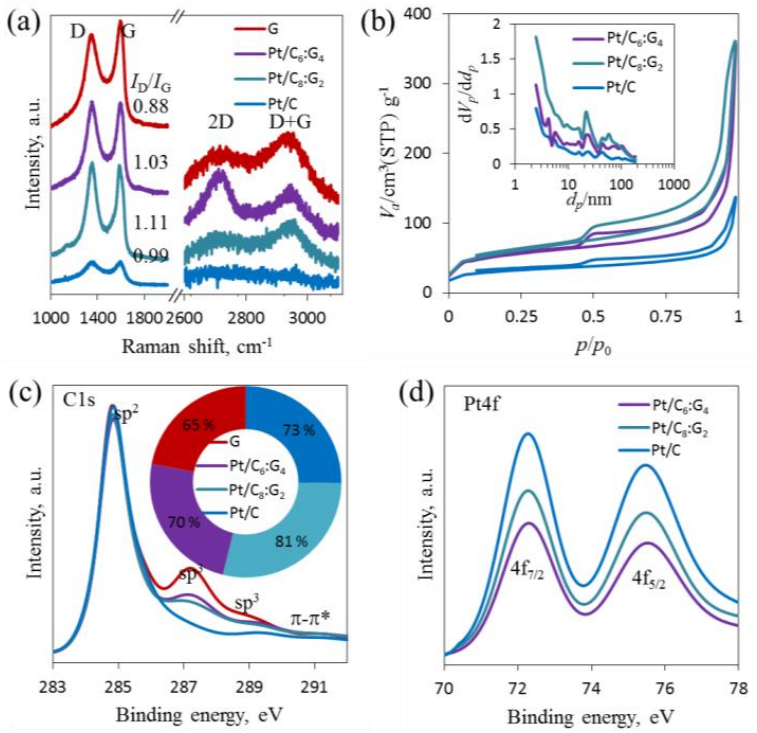

Figure 3. Raman spectroscopy (**a**), nitrogen adsorption−desorption isotherms (**b**), core-level of C 1s (**c**) and Pt 4f XPS spectra for Pt/C, Pt/C_8:G_2 and Pt/C_6:G_4 (**d**); for comparison, G-sheets was analyzed by Raman and XPS. Insets: pore size distribution (using BJH method) (**b**) and the sp^2-C (%) of corresponding samples (**c**).

3.3. SSA Measurement of Pt/C_x:G_{10-x}

The porosity is an important characteristic that involves with the SSA and electrocatalytic properties of carbon-based materials [50,51]. The SSA and pore distribution of as prepared composite samples has been figured out by N_2 adsorption/desorption curves as can be seen in Figure 3b. The type-IV isothermal curves are confirmed the presence of mesopores in all composite samples [52]. Therefore, the SSA (trough Brunaue–Emmett–Teller method) of Pt/C_8:G_2 was measured as 471 m^2 g^{-1}, which was significantly greater than the Pt/C_6:G_4 (423 m^2 g^{-1}) and the Pt/C (318 m^2 g^{-1}). This is probably due to the few layer G-sheets assembly and the less aggregation of carbon black compared to Pt/C_6:G_4 and Pt/C, respectively. The pore size distribution (using the Barrett–Joyner–Halenda method, BJH) curves derived from the N_2 desorption which confirming the presence of the abundant pores in Pt/C_8:G_2 sample with average pore diameter of 10.3 nm and a pore volume of 1.8 cm^3 g^{-1} (Figure 3b inset). Both values were much lower for Pt/C_6:G_4 and Pt/C samples. Therefore, larger SSA, higher pore volume and wider range of pore size distribution are indicating that of facile electrocatalysis at Pt/C_8:G_2 than those of Pt/C_6:G_4 and Pt/C samples.

3.4. XPS Analysis of Pt/C_x:G_{10-x}

The X-ray photoelectron spectroscopy (XPS) analysis has been used to reach further insight into the composite formation as well as the elemental analysis. In Figure S1, mainly three peaks appeared in XPS survey spectra of Pt-containing samples at ~70 eV, ~284.1 eV and ~532.1 eV, which signify the presence of Pt, C and O elements, respectively [8,53], whereas the G-sheets XPS survey spectrum showed only C and O peaks. However, the C and O ratio (C/O, at%) was calculated as 17 for Pt/C, which was decreased to 7.6 and 6.3 for Pt/C_8:G_2 and Pt/C_6:G_4, respectively. Indicating significant amount of oxygen was incorporated in all composite samples due to addition of G-sheets [12] although,

C/O of G-sheets was 6.5. Additionally, the amount of Pt was confirmed as 20, 16.5 and 14.7 wt% in Pt/C, Pt/C_8:G_2 and Pt/C_6:G_4 samples, respectively.

For a detail analysis of distribution of carbonaceous groups in all samples, the core level of C 1s XPS spectra for Pt/C, Pt/C_8:G_2, Pt/C_6:G_4 and G-sheets are presented in Figures 2c and S2. The C 1s was deconvoluted by five different components (Figure S2) assigned to the oxygen-free sp^2-C (C=C) at 285.2 eV and oxygen containing sp^3-C, such as C–O at 285.7 eV, C=O at 287.4 eV and O–C=O at 289.2 eV with a π–π^* at 291.2 eV [15,43,54]. However, the C 1s spectrum of Pt/C shows only a sharp peak for sp^2-C, which signifies that a smaller amount of oxygen-containing species were presence in this sample. Compared to Pt/C, the high intensity peak appeared at other C 1s XPS spectra for sp^3-C species, which indicates that oxygen-species were gradually increased due to the gradual addition of G-sheets. Although the sp^2-C peak intensity showed a similar amount of sp^2-C in all samples, the detected sp^2-C species was higher in Pt/C_8:G_2 sample, as shown in the pie chart in Figure 2c inset. This pie chart describes the percentage of sp^2-C species was higher in Pt/C_8:G_2 sample among all samples possibly due to better reduction with limited addition of G-sheets. Finally, the comparative Pt 4f XPS spectra for Pt/C, Pt/C_8:G_2 and Pt/C_6:G_4 are shown in Figures 3d and S3. In Figure 3d, all Pt 4f spectra present a doublet consisting with two bands at 72.3 and 75.5 eV, which were assigned to the Pt $4f_{7/2}$ and Pt $4f_{5/2}$, respectively. The distribution of Pt metallic states in those samples was displayed in Figure S3, which confirms to that all Pt in those samples were mostly in Pt^0 state. However, both Pt $4f_{7/2}$ and Pt $4f_{5/2}$ peak positions of those samples were in the same position even upon addition of G-sheet, indicating that all PtNPs in those samples were in the same electronic environment and no significant change was observed due to G-sheet addition, except reducing total Pt content.

3.5. Electrochemical Analysis of Pt/C_x:G_{10-x}

The Pt/C_x:G_{10-x} catalysts were placed onto clean GCE with different Pt-mass loading, the electrochemical measurements were then carried out by CV technique in Ar-saturated 0.1 M $HClO_4$ solution as displayed in Figure 4a. The Figure 4a exhibitions CV curves which recorded on Pt/C, Pt/C_8:G_2 and Pt/C_6:G_4, respectively, in the potential range of 1.2 to 0 V (versus RHE) at a fixed scan rate of 50 mV s^{-1}. The PtO reduction peak located around 0.7 V and the H_2 adsorption/desorption peaks at the range of 0.4 to 0 V in the backward CV scan was clearly appeared in all curves. The electrochemical surface area (ECSA) of all Pt-containing catalysts was derived from the Coulombic charge (Q) that are associated with H_2 adsorption-desorption on Pt-site using Equation (1) [55,56]. The ECSA of Pt-containing catalysts was calculated as 63, 77 and 65 m^2 g_{Pt}^{-1}, while the Pt-loading was 28.3, 23.3 and 20.8 μg_{Pt} cm^{-2} for the Pt/C, Pt/C_8:G_2 and Pt/C_6:G_4, respectively. The obtained ECSA for Pt/C_8:G_2 was significantly higher than those of Pt/C and Pt/C_6:G_4, which indicates that the Pt-site in Pt/C_8:G_2 was much exposed and electroactive. It is well known that the ECSA value is an important indication of the precious metals utilization with minimal metal loading. Therefore, this result signifies a better utilization of active Pt-sites in Pt/C_8:G_2 catalyst probably due to the higher SSA, better dispersion of Pt NPs with less dissolution nature.

$$\text{ECSA} = Q_o/(Q_r \times m) \quad (1)$$

where Q_o is the charge associated with the H_2 adsorption/desorption region, Q_r is the charge required for the monolayer adsorption of H_2 on Pt surface (assumed to be 210 μC cm^{-2}) [55,56] and m is the Pt-mass loading (in μg cm^{-2}).

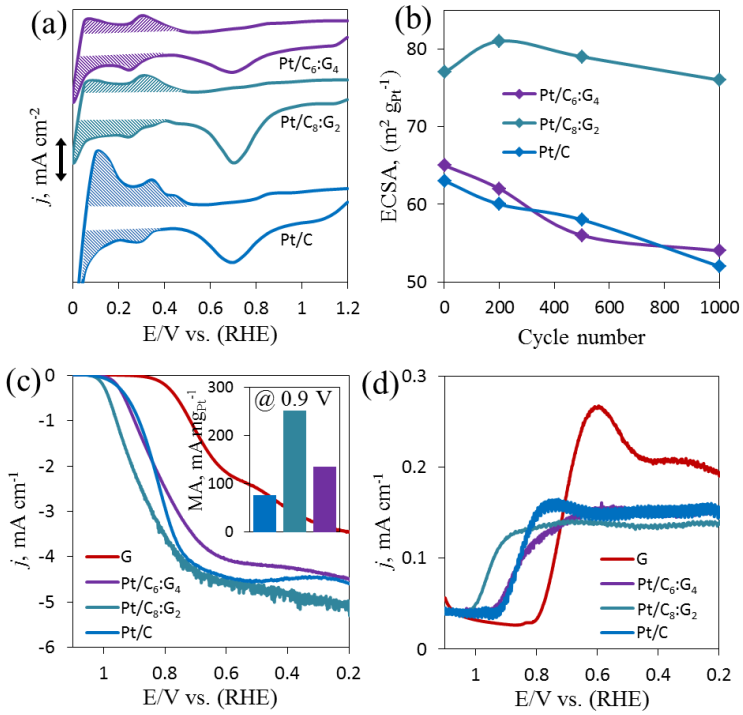

Figure 4. Cyclic voltammetry (CV) curves at a scan rate of 50 mV s^{-1} (scale bar: 1 mA cm^{-2}) (**a**) and change of electrochemically active surface area (ECSA) during the accelerated durability test by CV (**b**) on Pt/C, Pt/C_8:G_2, and Pt/C_6:G_4 electrodes in an Ar-saturated 0.1 M $HClO_4$ electrolyte, the rotating ring disk electrode (RRDE) curves for the oxygen reduction reaction (ORR) at a scan rate of 5 mV s^{-1} at the disc electrode (**c**) and at the ring electrode (**d**) on above mentioned electrodes including G-sheets-modified electrodes in O_2-saturated 0.1 M $HClO_4$ electrolyte. Inset: the mass activity (MA) comparison at 0.9 V (versus reversible hydrogen electrode (RHE)) for all Pt-containing electrodes.

The electrochemical stability of catalysts under practical operating condition is a key factor for commercialization and extensive use of FCs. The CV experiment was performed for evaluating longterm ECSA stability and the variation of ECSA has shown in Figure 4b. In Figure 4b, for Pt/C_8:G_2, the initial value was 77 m^2 g_{Pt}^{-1}, which increased to 81 and 79 m^2 g_{Pt}^{-1} in the first 200 and 500 cycles, respectively, and finally decreased to 76 m^2 g_{Pt}^{-1} after 1000 cycles. The ECSA of Pt/C dropped at 60 m^2 g_{Pt}^{-1} from its initial ECSA (63 m^2 g_{Pt}^{-1}) after 200 cycles, and the final ECSA after 1000 cycles dropped to 52 m^2 g_{Pt}^{-1}. Similarly, the ECSA of Pt/C_6:G_4 dropped at 54 m^2 g_{Pt}^{-1} after 1000 cycles from 65 m^2 g_{Pt}^{-1} as this was its initial ECSA. Thus, the Pt/C_8:G_2 demonstrated a good ECSA stability up to the 1000 CV cycles which was significantly higher than the benchmark carbon supported Pt/C.

3.6. Electrochemical ORR on Pt/C_x:G_{10-x}

For exploring the catalytic activity of the Pt/C_x:G_{10-x} composite catalysts for electrochemical ORR, the LSV curves on RRDE were then recorded for Pt/C, Pt/C_8:G_2, Pt/C_6:G_4 and G-sheets electrodes in O_2-saturated 0.1 M $HClO_4$ solution at a scan rate of 5 mV s^{-1} and at a constant rotation speed (1600 rpm), which are shown in Figure 4c. As can be seen in Figure 4c, the onset potential (E_{onset}) of ORR for the Pt/C electrode was at 0.95 V (versus RHE) and the limiting diffusion current density (j_L) was 4.47 mA cm^{-2} at 0.4 V (versus RHE). Upon the addition of G-sheets, the ORR E_{onset} shifted positively to 1.01 V, which was accompanied by a concomitant increase in the ORR j_L up to 4.8 mA cm^{-2} at 0.4 V (versus RHE) on Pt/C_8:G_2 electrode, indicating an improved ORR catalysis on Pt/C_8:G_2 electrode in terms of both parameters. However, the excess amount of G-sheets addition the ORR activity decreased in respect to the E_{onset} and j_L on Pt/C_6:G_4 electrode (0.95 V and 4.24 mA cm^{-2}) and both parameters were tremendously decreased on G-sheets electrode (0.9 V and 3 mA cm^{-2}) (E_{onset}

confirmed from Figure S4). These results clearly demonstrated a significant enhancement in the ORR electrocatalytic activity for the Pt/C_8:G_2 than not only the Pt/C_6:G_4 and G-sheets electrodes but also the pure benchmark Pt/C electrode.

To compare the electrocatalytic activity towards ORR against Pt-mass, the Pt-mass normalized kinetic current density (j_k) was calculated at 0.9 V (versus RHE) in Figure 4c inset. The Pt/C_8:G_2 catalyst provided the highest MA (252 mA mg_{Pt}^{-1}) towards ORR which was 3.3 and 1.9 times greater than those of Pt/C (76.5 mA μg_{Pt}^{-1}) and Pt/C_6:G_4 (135.6 mA μg_{Pt}^{-1}), respectively. This is consistent with the significantly higher specific activity (SA, ECSA normalized j_k) at 0.9 V (versus RHE) for ORR at Pt/C_8:G_2 (0.27 mA cm_{ECSA}^{-2}) than those of Pt/C (0.12 mA cm_{ECSA}^{-2}) and Pt/C_6:G_4 (0.15 mA cm_{ECSA}^{-2}) electrodes as shown in Figure S5. In addition, LSV curves of ring electrode on RRDE for Pt/C, Pt/C_8:G_2, Pt/C_6:G_4 and G-sheets electrodes have been compared in Figure 4d. The ring current density was produced from the generation of H_2O_2 during ORR [57,58]. As can be seen, all electrodes started to generate the ring current at the E_{onset} of ORR and the intensity of steady state current region indicated the degree of H_2O_2 generation. However, on the Pt/C_8:G_2 electrode, the H_2O_2 generation was significantly less than that on other electrodes which is favorable for ORR process, indicating that Pt/C_8:G_2 was comparatively better electrocatalyst towards ORR. Therefore, the electrochemical results show that the Pt/C_8:G_2 was efficient electrocatalyst than those of other tested electrodes in respect to the E_{onset}, MA, and SA towards ORR because of the higher porosity, larger SSA and improved ECSA.

3.7. Kinetics of ORR on Pt/C_x:G_{10-x}

It is known that the ORR in aqueous solution occurs mainly by two pathways: the direct four-electron reduction pathway from O_2 to H_2O and the two-electron reduction pathway from O_2 to H_2O_2 [59]. However, to evaluate the ORR pathway on Pt/C, Pt/C_8:G_2, Pt/C_6:G_4 and G-sheets electrodes, the RRDE data was then used for the calculation of transferred electron numbers per O_2 (n) and the corresponding H_2O_2 formation on aforementioned electrodes during the ORR process from Equations (1) and (2) [60,61] in Figure 5a. As shown in Figure 5a, the n value was found to be dependent on the potential for all electrodes. Initially, the n value rapidly increased afterwards slowly increased with the subsequent potential range. However, the n for ORR at the Pt/C_8:G_2 electrode (3.95 to 4.02) was always higher than those on commercial Pt/C (3.85 to 3.92), Pt/C_6:G_4 (3.83 to 3.89) and G-sheets (3 to 3.6) at the potential range of 0.8 V to 0.2 V. Therefore, the ORR proceeded via a four-electron pathway at Pt/C_8:G_2 electrode which was even better than those of other tested electrodes in this study [62]. This is consistent with the relatively lower H_2O_2 production during ORR at the Pt/C_8:G_2 electrode with compared to those electrodes (Figure 5b). Therefore, it has been confirmed that the Pt/C_8:G_2 composite electrode was comparatively better ORR electrocatalyst than Pt/C and other tested electrodes in respect to the higher number of electron transfer per O_2 as well as a lower production of H_2O_2.

$$n = \frac{4i_d}{i_d + \left(\frac{i_r}{N}\right)} \tag{2}$$

$$H_2O_2\ \% = \frac{200\frac{i_r}{N}}{i_d + \frac{i_r}{N}} \tag{3}$$

$$N = \frac{-i_r}{i_d} \tag{4}$$

where i_d and i_r are the disk and ring electrode currents, respectively, and N is the collection efficiency of the RRDE (0.37), as calculated from Equation (3).

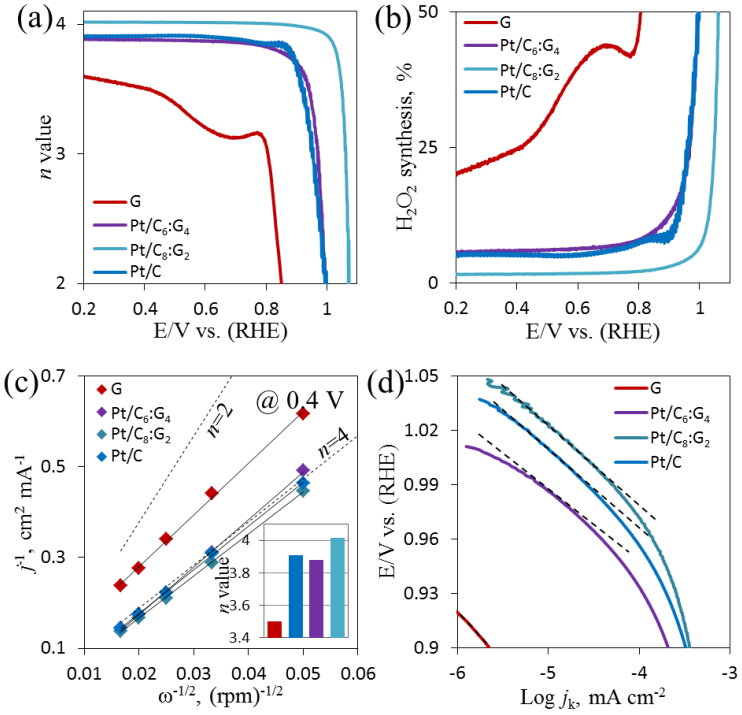

Figure 5. The calculated transferred electron number (**a**), the corresponding H_2O_2 synthesis (**b**) during ORR in O_2-saturated 0.1 M $HClO_4$ solution, the K-L plot comparison at 0.4 V (versus RHE) (**c**) and the Tafel plots (**d**) for Pt/C, Pt/C_8:G_2, Pt/C_6:G_4 and G-sheets electrodes. Inset: the K-L plot derived transferred electron number at 0.4 V (versus RHE).

To gain further insight into the ORR electrocatalysis on Pt/C_x:G_{10-x} and G-sheets electrodes, the reaction kinetics were investigated by RDE at various rotation speeds in same electrolyte (Figure S6). In Figure S6, the LSV curves showed that the limiting current density (*j*) of ORR was increased by the increasing rotating speed in all cases. At a constant rotation rate, upon controlled addition of G-sheets with Pt/C, the *j* of ORR at the Pt/C_8:G_2 electrode was always higher than those of other tested electrodes, indicating an improved ORR process at Pt/C_8:G_2 electrode. However, the Koutecky–Levich (K–L) plots resultant from the corresponding LSV curves showed the linear relationships between j_L^{-1} and angular velocity ($\omega^{-1/2}$, $\omega = 2\pi^*$ rpm) for all electrodes at various potentials (0.6 V to 0.2 V versus RHE). Particularly, the K–L plots for Pt/C_8:G_2 electrode (Figure S6) maintained nearly same slopes over the potential range was studied in respect to the K–L plots for other tested electrodes, indicating a consistent number of electron transferred per O_2 molecule during ORR and comparatively better first-order reaction kinetic ORR possess on Pt/C_8:G_2 electrode than Pt/C, Pt/C_6:G_4 and G-sheets electrodes [63,64]. However, for a better understanding, the comparison of K-L plots and *n*-values (calculated from K-L slopes) at 0.4 V (versus RHE) are also presented for all catalysts in Figure 5c. As can be seen in Figure 5c, all K-L plots were parallel and near to the dotted line that represented to the theoretical value of four-electron involved ORR. Particularly, the K-L plot of Pt/C_8:G_2 electrode was much betted parallel to the four-electron line, indicating a higher n-value towards ORR at any rotation speed. The n-value for ORR at the Pt/C_8:G_2 electrode (4.02) was higher than those on Pt/C (3.91), Pt/C_6:G_4 (3.88) and G-sheets (3.5) at 0.4 V (versus RHE) (Figure 5c inset). These values were concomitant to the previous calculation.

To analyze the Tafel behavior, the Tafel plots were derived for further kinetic investigation for all catalysts in Figure 5d. As shown in Figure 5d, the Tafel slope for Pt/C_8:G_2 electrode was 63 mV dec^{-1} at a low overpotential which was very close to the theoretical value and Pt/C (62 mV dec^{-1}), and obviously better than the Pt/C_6:G_4 (72 mV dec^{-1}) and G-sheets (91 mV dec^{-1}). The result also indicated a better ORR catalysis on Pt/C_8:G_2 catalyst with improved ORR mechanism and faster electron transfer.

3.8. Stability and Selectivity Towards ORR on Pt/C_x:G_{10-x}

The Pt/C_8:G_2, Pt/C_6:G_4 and Pt/C electrodes were further subjected to investigate the stability and selectivity toward ORR which is regarded as the key factor for the widespread commercialization of FCs. The stability of those electrodes was evaluated during ORR through CA technique at 0.8 V (RHE) in an O_2- saturated 0.1 M $HClO_4$ at a rotation rate of 1600 rpm in Figure 6a. As depicted in Figure 6a, the relative current from all electrodes decreased with time and the Pt/C_8:G_2 electrode showed a slower decrease at ~25% after continuous reaction for 30,000 s, whereas the Pt/C_6:G_4 and Pt/C clearly decreased to ~48% and ~45%, respectively, at the same time, indicating that the Pt/C_8:G_2 electrocatalyst was approximately two times higher stable than the commercial Pt/C and Pt/C_6:G_4 electrodes. Additionally, the possible crossover effect was also investigated in presence of anodic fuel molecules (e.g., ethanol, methanol) during ORR at the Pt/C, Pt/C_6:G_4 and Pt/C_8:G_2 electrodes as in Figure 6b. As described in Figure 6b, a sharp response and huge decease in relative current was observed in CA curve for the Pt/C electrode and considerably lower decease in relative current was observed in CA curve for the Pt/C_6:G_4 electrode upon addition of 2 M ethanol and methanol, respectively. However, the CA curve for the Pt/C_8:G_2 electrode was slightly changed in relative current upon addition of ethanol and methanol, indicating that the Pt/C_8:G_2 electrocatalyst was better selective toward ORR and resistive to the crossover effect than the commercial Pt/C and Pt/C_6:G_4 electrocatalysts.

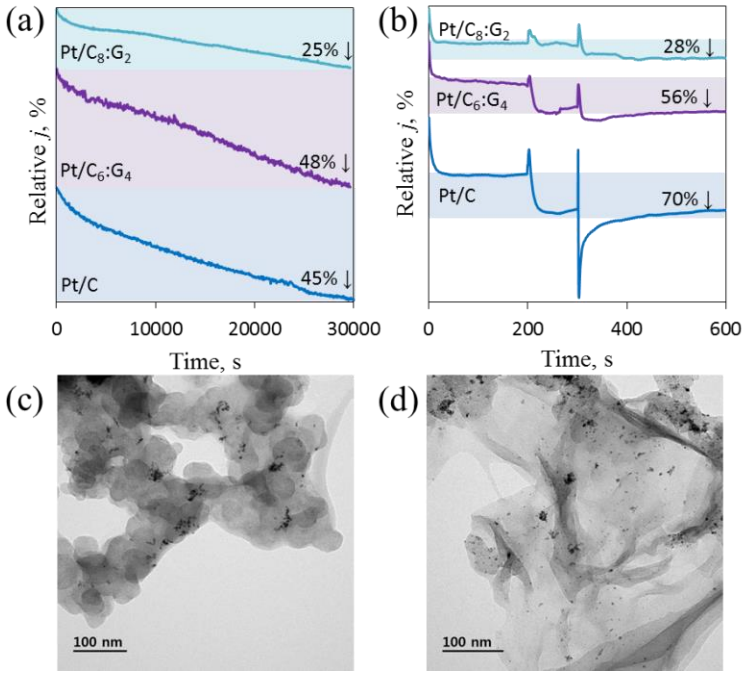

Figure 6. The chronoamperometry (CA) responses for ORR at the Pt/C and Pt/C_8:G_2 electrodes for long term stability test (**a**) and selectivity test (**b**) with the addition of 2 M ethanol and methanol, respectively, in an O_2-saturated 0.1 M $HClO_4$ solution at 1600 rpm rotation speed and at an applied potential of 0.8 V (versus RHE); a comparison of TEM images of Pt/C (**c**), and Pt/C_8:G_2 (**d**) after long-term stability test.

Finally, the morphology of Pt/C (Figure 6c) and Pt/C_8:G_2 (Figure 6d) was evaluated by TEM analysis after a stability test via CA. As can be seen, Pt NPs were found to be detached from the carbon support with higher agglomeration in Pt/C catalyst (Figure 6c) as a result of severe dissolution and corrosion of carbon support [65]. On the other hand, the Pt/C_8:G_2 composite catalyst achieved a more uniform Pt NPs distribution after the stability test and Pt NPs were not detached from the graphene and carbon support (Figures 6d and S7). Therefore, all described results confirmed that the Pt/C_8:G_2 composite catalyst is much efficient ORR catalyst in terms of better electrocatalysis, stability and fuel selectivity among Pt/C_x:G_{10-x} including Pt/C.

4. Conclusions

Finally, the Pt/C with G-sheets composite could act as an efficient ORR electrocatalyst, which was prepared through a simple composite making. The optimum ration of carbon and graphene composite exhibited stable ECSA with minimal Pt-loading which resultant from higher SSA and aggregation-free dispersion of Pt NPs. As a result, Pt/C_8:G_2 catalyst showed superior activity toward ORR in respect to the not only high E_{onset}, limiting current, MA and SA but also high stability and resistance to the crossover effect. Notably, the Pt/C_8:G_2 composite catalyst showed significantly better ORR kinetics with lowering H_2O_2 formation and higher long-term operational stability than that of benchmark Pt/C and other composite electrodes.

Supplementary Materials: The following are available online at http://www.mdpi.com/2227-9717/7/9/586/s1, Figure S1: XPS survey spectra for Pt/C, Pt/C_8:G_2, Pt/C_6:G4 and Pt/C_1:G_9 samples. Figure S2: C 1s XPS spectra for Pt/C (a), Pt/C_8:G_2 (b), Pt/C_6:G_4 (c) and G-sheets (d) samples. Figure S3: Pt 4f XPS spectra for Pt/C (a), Pt/C_8:G_2 (b) and Pt/C_6:G_4 (c) samples. Figure S4: Curves showing the ORR onset potential for Pt/C_8:G_2 (a), Pt/C_6:G_4 (b), Pt/C (c) and G-sheets (d) electrodes. Figure S5: Comparison of MA and SA for Pt/C, Pt/C_8:G_2 and Pt/C_6:G_4 electrodes at 0.9 V. Figure S6: LSV curves for ORR at various rpm on G-sheets (a), Pt/C (c), Pt/C_8:G_2 (e) and Pt/C_6:G_4 (g) electrodes in an O_2-saturated 0.1 M $HClO_4$ electrolyte at a scan rate of 5 mV s^{-1}; the corresponding K-L plots for G-sheets (b), Pt/C (d), Pt/C_8:G_2 (f) and Pt/C_6:G_4 (h) at different electrode potentials. Figure S7: Comparison of TEM images of Pt/C (a, c), and Pt/C_8:G_2 (b, d) before (a, b) and after (c, d) long-term stability test.

Author Contributions: H.B. has done all electrochemical experiments, wrote this manuscript and analyzed all the results in due discussion with Y.-B.K. Additionally, H.B. and Y.-B.K. both designed the experiments.

Funding: This work was supported by the National Research Foundation of Korea (15R1A4A1041746 and 18R1D1A1B07044005).

Conflicts of Interest: The authors declare no conflict of interest.

References

1. Debe, M.K. Electrocatalyst approaches and challenges for automotive fuel cells. *Nature* **2012**, *486*, 43–51. [CrossRef] [PubMed]
2. Yu, W.; Porosoff, M.D.; Chen, J.G. Review of Pt-based bimetallic catalysis: From model surfaces to supported catalysts. *Chem. Rev.* **2012**, *112*, 5780–5817. [CrossRef] [PubMed]
3. Chen, J.Y.; Lim, B.; Lee, E.P.; Xia, Y.N. Shape-controlled synthesis of platinum nanocrystals for catalytic and electrocatalytic applications. *Nano Today* **2009**, *4*, 81–95. [CrossRef]
4. Wu, J.; Yang, H. Platinum-based oxygen reduction electrocatalysts. *Acc. Chem. Res.* **2013**, *46*, 1848–1857. [CrossRef] [PubMed]
5. Lee, K.; Ahmed, M.S.; Jeon, S. Electrochemical deposition of silver on manganese dioxide coated reduced graphene oxide for enhanced oxygen reduction reaction. *J. Power Sources* **2015**, *288*, 261. [CrossRef]
6. Markovic, N.M.; Grgur, B.N.; Ross, P.N. Temperature-dependent hydrogen electrochemistry on platinum low-index single-crystal surfaces in acid solutions. *J. Phys. Chem. B* **1997**, *101*, 5405–5413. [CrossRef]
7. Paulus, U.A.; Schmidt, T.J.; Gasteiger, H.A.; Behm, R.J. Oxygen reduction on a high-surface area Pt/Vulcan carbon catalyst: A thin-film rotating ring-disk electrode study. *J. Electroanal. Chem.* **2001**, *495*, 134–145. [CrossRef]
8. Ahmed, M.S.; Kim, D.; Jeon, S. Covalently grafted platinum nanoparticles to multi walled carbon nanotubes for enhanced electrocatalytic oxygen reduction. *Electrochimca Acta* **2013**, *92*, 168. [CrossRef]
9. Lim, B.; Jiang, M.; Camargo, P.H.C.; Cho, E.C.; Tao, J.; Lu, X.; Zhu, Y.; Xia, Y. Pd-Pt bimetallic nanodendrites with high activity for oxygen reduction. *Science* **2009**, *324*, 1302. [CrossRef] [PubMed]
10. Choe, J.E.; Ahmed, M.S.; Jeon, S. 3,4-ethylenedioxythiophene functionalized graphene with palladium nanoparticles for enhanced electrocatalytic oxygen reduction reaction. *J. Power Sources* **2015**, *281*, 211. [CrossRef]
11. Dong, Y.; Zhou, Y.W.; Wang, M.Z.; Zheng, S.L.; Jiang, K.; Cai, W.B. Facile aqueous phase synthesis of carbon supported B-doped Pt_3Ni nanocatalyst for efficient oxygen reduction reaction. *Electrochimca Acta* **2017**, *246*, 242. [CrossRef]
12. Ahmed, M.S.; Jeon, S. Highly active graphene-supported Ni_xPd_{100-x} binary alloyed catalysts for electro-oxidation of ethanol in an alkaline media. *ACS Catal.* **2014**, *4*, 1830. [CrossRef]

13. Begum, H.; Ahmed, M.S.; Lee, D.W.; Kim, Y.B. Carbon nanotubes-based PdM bimetallic catalysts through N_4-system for efficient ethanol oxidation and hydrogen evolution reaction. *Sci. Rep.* **2019**, *9*, 11051. [CrossRef] [PubMed]
14. Wang, A.J.; Liu, L.; Lin, X.X.; Yuan, J.; Feng, J.J. One-pot synthesis of 3D freestanding porous PtAg hollow chain-like networks as efficient electrocatalyst for oxygen reduction reaction. *Electrochimca Acta* **2017**, *245*, 883. [CrossRef]
15. Begum, H.; Ahmed, M.S.; Jeon, S. A novel δ-MnO_2 with carbon nanotubes nanocomposite as an enzyme-free sensor for hydrogen peroxide electrosensing. *RSC Adv.* **2016**, *6*, 50572. [CrossRef]
16. Bregoli, L.J. The influence of platinum crystallite size on the electrochemical reduction of oxygen in phosphoric acid. *Electrochimca Acta* **1978**, *23*, 489–492. [CrossRef]
17. Kinoshita, K. Particle size effects for oxygen reduction on highly dispersed platinum in acid electrolytes. *J. Electrochem. Soc.* **1990**, *137*, 845–848. [CrossRef]
18. Wang, Y.J.; Zhao, N.; Fang, B.; Li, H.; Bi, X.T.; Wang, H. Carbon-supported Pt-based alloy electrocatalysts for the oxygen reduction reaction in polymer electrolyte membrane fuel cells: Particle size, shape, and composition manipulation and their impact to activity. *Chem. Rev.* **2015**, *115*, 3433–3467. [CrossRef]
19. Peng, Z.; Yang, H. Designer platinum nanoparticles: Control of shape, composition in alloy, nanostructure and electrocatalytic property. *Nano Today* **2009**, *4*, 143–164. [CrossRef]
20. Darling, R.M.; Meyers, J.P. Kinetic model of platinum dissolution in PEMFCs. *J. Electrochem. Soc.* **2003**, *150*, A1523–A1527. [CrossRef]
21. Van der Vliet, D.F.; Wang, C.; Li, D.; Paulikas, A.P.; Greeley, J.; Rankin, R.B.; Strmcnik, D.; Tripkovic, D.; Markovic, N.M.; Stamenkovic, V.R. Unique electrochemical adsorption properties of Pt-skin surfaces. *Angew. Chem. Int. Ed.* **2012**, *51*, 3139–3142. [CrossRef] [PubMed]
22. Cui, C.; Gan, L.; Heggen, M.; Rudi, S.; Strasser, P. Compositional segregation in shaped Pt alloy nanoparticles and their structural behavior during electrocatalysis. *Nat. Mater.* **2013**, *12*, 765–771. [CrossRef] [PubMed]
23. Li, M.; Zhao, Z.; Cheng, T.; Fortunelli, A.; Chen, C.-Y.; Yu, R.; Zhang, Q.; Gu, L.; Merinov, B.V.; Lin, Z.; et al. Ultrafine jagged platinum nanowires enable ultrahigh mass activity for the oxygen reduction reaction. *Science* **2016**, *354*, 1414–1419. [CrossRef] [PubMed]
24. Wang, C.; Markovic, N.M.; Stamenkovic, V.R. Advanced platinum alloy electrocatalysts for the oxygen reduction reaction. *ACS Catal.* **2012**, *2*, 891–898. [CrossRef]
25. Zhang, L.; Zhu, S.; Chang, Q.; Su, D.; Yue, J.; Du, Z.; Shao, M. Palladium−platinum core−shell electrocatalysts for oxygen reduction reaction prepared with the assistance of citric acid. *ACS Catal.* **2016**, *6*, 3428–3432. [CrossRef]
26. Yang, J.; Kim, S.H.; Kwak, S.K.; Song, H.K. Curvature-induced metal-support interaction of an islands-byislands composite of platinum catalyst and carbon nano-onion for durable oxygen reduction. *ACS Appl. Mater. Interfaces* **2017**, *9*, 23302–23308. [CrossRef] [PubMed]
27. Begum, H.; Ahmed, M.S.; Cho, S.; Jeon, S. Simultaneous reduction and nitrogen functionalization of graphene oxide using lemon for metal-free oxygen reduction reaction. *J. Power Sources* **2017**, *372*, 116–124. [CrossRef]
28. Balandin, A.A.; Ghosh, S.; Bao, W.; Calizo, I.; Teweldebrhan, D.; Miao, F.; Lau, C.N. Superior thermal conductivity of single-layer graphene. *Nano Lett.* **2008**, *8*, 902–907. [CrossRef] [PubMed]
29. Morozov, S.V.; Novoselov, K.S.; Katsnelson, M.I.; Schedin, F.; Elias, D.C.; Jaszczak, J.A.; Geim, A.K. Giant intrinsic carrier mobilities in graphene and its bilayer. *Phys. Rev. Lett.* **2008**, *100*, 016602. [CrossRef] [PubMed]
30. Ahmed, M.S.; Han, H.S.; Jeon, S. One-step chemical reduction of graphene oxide with oligothiophene for improved electrocatalytic oxygen reduction reactions. *Carbon* **2013**, *61*, 164–172. [CrossRef]
31. Begum, H.; Ahmed, M.S.; Jeon, S. New Approach for porous chitosan−graphene matrix preparation through enhanced amidation for synergic detection of dopamine and uric acid. *ACS Omega* **2017**, *2*, 3043–3054. [CrossRef] [PubMed]
32. Ahmed, M.S.; Kim, Y.B. Amide-functionalized graphene with 1,4-diaminobutane as efficient metal-free and porous electrocatalyst for oxygen reduction. *Carbon* **2017**, *111*, 577–586. [CrossRef]
33. Hu, C.; Xue, J.; Dong, L.; Jiang, Y.; Wang, X.; Qu, L.; Dai, L. Scalable preparation of multifunctional fire retardant ultralight graphene foams. *ACS Nano* **2016**, *10*, 1325–1332. [CrossRef] [PubMed]

34. Men, B.; Sun, Y.; Li, M.; Hu, C.; Zhang, M.; Wang, L.; Tang, Y.; Chen, Y.; Wan, P.; Pan, J. Hierarchical Metal-free nitrogen-doped porous graphene/carbon composites as an efficient oxygen reduction reaction catalyst. *ACS Appl. Mater. Interfaces* **2016**, *8*, 1415–1423. [CrossRef] [PubMed]
35. Huang, J.; Wang, J.; Wang, C.; Zhang, H.; Lu, C.; Wang, J. Hierarchical porous graphene carbon-based supercapacitors. *Chem. Mater.* **2015**, *27*, 2107–2113. [CrossRef]
36. Higgins, D.C.; Hoque, M.A.; Hassan, F.; Choi, J.Y.; Kim, B.; Chen, Z. Oxygen reduction on graphene−carbon nanotube composites doped sequentially with nitrogen and sulfur. *ACS Catal.* **2014**, *4*, 2734–2740. [CrossRef]
37. Allen, M.J.; Tung, V.C.; Kaner, R.B. Honeycomb carbon: A review of graphene. *Chem. Rev.* **2010**, *110*, 132–145. [CrossRef]
38. Probst, N.; Grivei, E. Structure and electrical properties of carbon black. *Carbon* **2002**, *40*, 201–205. [CrossRef]
39. Tao, L.; Wang, Q.; Dou, S.; Ma, Z.; Huo, J.; Wang, S.; Dai, L. Edge-rich and dopant-free graphene as a highly efficient metal-free electrocatalyst for the oxygen reduction reaction. *Chem. Commun.* **2016**, *52*, 2764–2767. [CrossRef]
40. Yang, H.B.; Miao, J.; Hung, S.F.; Chen, J.; Tao, H.B.; Wang, X.; Zhang, L.; Chen, R.; Gao, J.; Chen, H.M.; et al. Identification of catalytic sites for oxygen reduction and oxygen evolution in N-doped graphene materials: Development of highly efficient metal-free bifunctional electrocatalyst. *Sci. Adv.* **2016**, *2*, e1501122. [CrossRef]
41. Sanetuntikul, J.; Hang, T.; Shanmugam, S. Hollow nitrogen-doped carbon spheres as efficient and durable electrocatalysts for oxygen reduction. *Chem. Commun.* **2014**, *50*, 9473–9476. [CrossRef] [PubMed]
42. Li, R.; Wei, Z.; Gou, X. Nitrogen and phosphorus dual-doped graphene/carbon nanosheets as bifunctional electrocatalysts for oxygen reduction and evolution. *ACS Catal.* **2015**, *5*, 4133–4142. [CrossRef]
43. Ahmed, M.S.; Jeon, S. Electrochemical activity evaluation of chemically damaged carbon nanotube with palladium nanoparticles for ethanol oxidation. *J. Power Sources* **2015**, *282*, 479–488. [CrossRef]
44. You, J.M.; Ahmed, M.S.; Han, H.S.; Choe, J.E.; Üstündag, Z.; Jeon, S. New approach of nitrogen and sulfur-doped graphene synthesis using dipyrrolemethane and their electrocatalytic activity for oxygen reduction in alkaline media. *J. Power Sources* **2015**, *275*, 73–79. [CrossRef]
45. Joo, Y.; Ahmed, M.S.; Han, H.S.; Jeon, S. Preparation of electrochemically reduced graphene oxide-based silver-cobalt alloy nanocatalysts for efficient oxygen reduction reaction. *Int. J. Hydrogen Energy* **2017**, *42*, 21751–21761. [CrossRef]
46. Marcano, D.C.; Kosynkin, D.V.; Berlin, J.M.; Sinitskii, A.; Sun, Z.; Slesarev, A.; Alemany, L.B.; Lu, W.; Tour, J.M. Improved synthesis of graphene oxide. *ACS Nano* **2010**, *4*, 4806–4814. [CrossRef]
47. Rivera, L.M.; Fajardo, S.; Arévalo, M.C.; García, G.; Pastor, E. S-and N-doped graphene nanomaterials for the oxygen reduction reaction. *Catalysts* **2017**, *7*, 278–290. [CrossRef]
48. Wen, Z.; Wang, X.; Mao, S.; Bo, Z.; Kim, H.; Cui, S.; Lu, G.; Feng, X.; Chen, J. Crumpled nitrogen-doped graphene nanosheets with ultrahigh pore volume for high-performance supercapacitor. *Adv. Mater.* **2012**, *24*, 5610–5616. [CrossRef]
49. Ke, Q.; Wang, J. Graphene-based materials for supercapacitor electrodes—A review. *J. Materiomics* **2016**, *2*, 37–54. [CrossRef]
50. Begum, H.; Ahmed, M.S.; Jeon, S. Highly efficient dual active palladium nanonetwork electrocatalyst for ethanol oxidation and hydrogen evolution. *ACS Appl. Mater. Interfaces* **2017**, *9*, 39303–39311. [CrossRef]
51. Ahmed, M.S.; Kim, Y.B. 3D graphene preparation via covalent amide functionalization for efficient metal-free electrocatalysis in oxygen reduction. *Sci. Rep.* **2017**, *7*, 43279. [CrossRef] [PubMed]
52. Begum, H.; Ahmed, M.S.; Cho, S.; Jeon, S. Freestanding palladium nanonetworks electrocatalyst for oxygen reduction reaction in fuel cells. *Int. J. Hydrogen Energy* **2018**, *43*, 229–238. [CrossRef]
53. Han, H.S.; Ahmed, M.S.; Jeong, H.; Jeon, S. Electrochemical sensing of monohydric alcohols on different linkers imbedded in between graphene and platinum nanoparticles. *J. Nanosci. Nanotechnol.* **2016**, *16*, 333–341. [CrossRef] [PubMed]
54. Ahmed, M.S.; Park, D.; Jeon, S. Ultrasmall $Pd_mMn_{1\_m}O_x$ binary alloyed nanoparticles on graphene catalysts for ethanol oxidation in alkaline media. *J. Power Sources* **2016**, *308*, 180–188. [CrossRef]
55. Zhao, Y.; Liu, J.; Zhao, Y.; Wang, F.; Song, Y. Pt–Co secondary solid solution nanocrystals supported on carbon as next-generation catalysts for the oxygen reduction reaction. *J. Mater. Chem. A* **2015**, *3*, 20086–20091. [CrossRef]

56. Ahmed, M.S.; Lee, D.W.; Kim, Y.B. Graphene supported silver nanocrystals preparation for efficient oxygen reduction in alkaline fuel cells. *J. Electrochem. Soc.* **2016**, *163*, F1169–F1176. [CrossRef]
57. Wang, C.H.; Huang, H.C.; Chang, S.T.; Lin, Y.C.; Huang, M.F. Pyrolysis of melamine-treated vitamin B12 as a non-precious metal catalyst for oxygen reduction reaction. *RSC Adv.* **2014**, *4*, 4207–4211. [CrossRef]
58. Ahmed, M.S.; Jeon, S. New functionalized graphene sheets for enhanced oxygen reduction as metal-free cathode electrocatalysts. *J. Power Sources* **2012**, *218*, 168–173. [CrossRef]
59. Ahmed, M.S.; Jeong, H.; You, J.M.; Jeon, S. Electrocatalytic reduction of dioxygen at a modified glassy carbon electrode based on Nafion-dispersed single-walled carbon nanotubes and cobalt–porphyrin with palladium nanoparticles in acidic media. *Electrochimca Acta* **2011**, *56*, 4924–4929. [CrossRef]
60. Ahmed, M.S.; Jeon, S. The nanostructure of nitrogen atom linked carbon nanotubes with platinum employed to the electrocatalytic oxygen reduction. *J. Nanosci. Nanotechnol.* **2013**, *13*, 306. [CrossRef]
61. Yun, M.; Ahmed, M.S.; Jeon, S. Thiolated graphene oxide-supported palladium cobalt alloyed nanoparticles as high performance electrocatalyst for oxygen reduction reaction. *J. Power Sources* **2015**, *293*, 380–387. [CrossRef]
62. Tang, X.; Ng, H.Y. Cobalt and nitrogen-doped carbon catalysts for enhanced oxygen reduction and power production in microbial fuel cells. *Electrochimca Acta* **2017**, *247*, 193. [CrossRef]
63. Sohn, G.J.; Choi, H.J.; Jeon, I.Y.; Chang, D.W.; Dai, L.; Baek, J.B. Water-dispersible, sulfonated hyperbranched poly(ether-ketone) grafted multiwalled carbon nanotubes as oxygen reduction catalysts. *ACS Nano* **2012**, *6*, 6345–6355. [CrossRef] [PubMed]
64. Park, D.; Ahmed, M.S.; Jeon, S. Covalent functionalization of graphene with 1,5-diaminonaphthalene and ultrasmall palladium nanoparticles for electrocatalytic oxygen reduction. *Int. J. Hydrogen Energy* **2017**, *42*, 2061–2070. [CrossRef]
65. Zhang, J.J.; Sui, X.L.; Huang, G.S.; Gu, D.M.; Wang, Z.B. Hierarchical carbon coated molybdenum dioxide nanotubes as a highly active and durable electrocatalytic support for methanol oxidation. *J. Mater. Chem. A* **2017**, *5*, 4067–4074. [CrossRef]